

Macroscopic Assembled Graphene for Silicon Mid-Infrared Photodetectors

Chao Gao (✉ chaogao@zju.edu.cn)

Zhejiang University

Li Peng

Zhejiang University

Sichao Du

Zhejiang University

Lixiang Liu

Zhejiang University

Srikrishna Bodepudi

Zhejiang University

Lingfei Li

Nanjing University <https://orcid.org/0000-0003-3573-6475>

Wei Liu

Zhejiang University <https://orcid.org/0000-0003-3894-0789>

Xin Cong

Chinese Academy of Sciences

Runchen Lai

Zhejiang University <https://orcid.org/0000-0002-5827-8991>

Wenzhang Fang

Zhejiang University

Xiaoxue Cao

Zhejiang University

Xinyu Liu

Zhejiang University

Muhammad Abid

Zhejiang University

Jianhang Lv

Zhejiang University

Junxue Liu

Chinese Academy of Sciences

Shengye Jin

Dalian Institute of Chemical Physics

Kaifeng Wu

Chinese Academy of Sciences

Qiaohui Zhou

Zhejiang University

Haiming Zhu

Zhejiang University <https://orcid.org/0000-0001-7747-9054>

Miao-Ling Lin

Chinese Academy of Sciences

Ping-Heng Tan

Chinese Academy of Sciences <https://orcid.org/0000-0001-6575-1516>

Qihua Xiong

Nanyang Technological University

Xiaomu Wang

Nanjing University <https://orcid.org/0000-0001-8975-5626>

Weida Hu

Shanghai Institute of Technical Physics, Chinese Academy of Sciences <https://orcid.org/0000-0001-5278-8969>

Xiangfeng Duan

University of California Los Angeles <https://orcid.org/0000-0002-4321-6288>

Bin Yu

Zhejiang University

Wenyan Yin

Zhejiang University

Zhen Xu

Zhejiang University <https://orcid.org/0000-0003-1352-9176>

Yang Xu

Zhejiang University <https://orcid.org/0000-0003-3148-7678>

Physical Sciences - Article

Keywords: Linear Energy Dispersion, Hot-electron Harvesting, Scalable Wet-assembly, Atomic-scale Contact Interface, Impact-ionization Avalanche Gain

Posted Date: November 30th, 2020

DOI: <https://doi.org/10.21203/rs.3.rs-75687/v1>

License:  This work is licensed under a Creative Commons Attribution 4.0 International License.

[Read Full License](#)

Macroscopic Assembled Graphene for Silicon Mid-Infrared Photodetectors

Li Peng^{1,10}, Sichao Du^{2,10}, Lixiang Liu^{2,10}, Srikrishna Chanakya Bodepudi², Lingfei Li², Wei Liu², Xin Cong³, Runchen Lai⁴, Wenzhang Fang¹, Xiaoxue Cao^{1,2}, Xinyu Liu², Muhammad Abid², Jianhang Lv², Junxue Liu⁴, Shengye Jin⁴, Kaifeng Wu⁴, Qiaohui Zhou⁵, Haiming Zhu⁵, Miao-Ling Lin³, Ping-Heng Tan³, Qihua Xiong⁶, Xiaomu Wang⁷, Weida Hu⁸, Xiangfeng Duan⁹, Bin Yu², Wenyan Yin², Zhen Xu¹, Yang Xu^{2*}, Chao Gao^{1*}

¹MOE Key Laboratory of Macromolecular Synthesis and Functionalization, Department of Polymer Science and Engineering, Zhejiang University, Hangzhou 310027, China.

²Colleges of ISEE and Microelectronics, State Key Laboratories of Modern Optical Instrumentation and Silicon Materials, Hangzhou Global Scientific and Technological Innovation Center, ZJU-UIUC Joint Institute, Zhejiang University, Hangzhou 310027, China

³State Key Laboratory of Superlattices and Microstructures, Institute of Semiconductors, Chinese Academy of Sciences, Beijing 100083, China

⁴State Key Laboratory of Molecular Reaction Dynamics and Dynamics, Dalian Institute of Chemical Physics, Chinese Academy of Sciences, Dalian 116023, China

⁵Department of Chemistry, Zhejiang University, Hangzhou 310027, China

⁶Division of Physics and Applied Physics, School of Physical and Mathematical Sciences, Nanyang Technological University, Singapore 637371, Singapore

⁷National Laboratory of Solid State Microstructures, Collaborative Innovation Center of Advanced Microstructure, School of Electronic Science and Engineering, Nanjing University, Nanjing 210093, China

⁸National Laboratory for Infrared Physics, Shanghai Institute of Technical Physics, Chinese Academy of Sciences, Shanghai 200083, China

⁹Department of Chemistry and Biochemistry, California Nanosystems Institute, University of California, Los Angeles 90095, USA

¹⁰These authors contributed equally: Li Peng, Sichao Du, Lixiang Liu

*e-mail: yangxu-isee@zju.edu.cn; chaogao@zju.edu.cn.

Graphene with linear energy dispersion and weak electron-phonon interaction is highly anticipated to harvest hot-electrons in a broad wavelength range from ultraviolet to terahertz^{1,2}. However, the limited absorption (~2.3%) and serious backscattering of hot-electrons associated with single-layer graphene result in inadequate quantum yields³⁻⁵, impeding their practically broadband photodetection, especially in the mid-infrared range. Here, we report a macroscopic assembled graphene (MAG)/silicon heterojunction for ultrafast mid-infrared photodetection. The highly crystalline 2-inch scale MAG with tunable thickness from 10 to 60 nm is produced by scalable wet-assembly of commercial graphene oxide followed by thermal annealing. The MAG/Si Schottky diode exhibits broadband photodetection capability in 1-10 μm at room temperature with fast response (120-130 ns, 4 mm² window) and high detectivity (10^{11} to 10^6 Jones), outperforming single-layer graphene/Si photodetectors by 2 to 8 orders in transient photocurrent. This optoelectronic performance is attributed to the superior advantages of MAG (~40% of light absorption, ~23 ps of carrier relaxation time, and high quasi-equilibrated hot-carrier-multiplication gain), atomic-scale contact interface of MAG and silicon, and impact-ionization avalanche gain (~ 10^2 times) from silicon. The MAG provides a long-range platform to understand the hot-carrier dynamics in stacked 2D materials, leading to next-generation broadband silicon-based image sensors.

Schottky junction, a kind of metal/semiconductor heterojunction, plays an important role in modern optoelectronics for high-speed optical communications and photodetection in visible and near-infrared (NIR) range^{6,7}. In mid-infrared (MIR) regime, the traditional metal-based Schottky junctions show high noise and low quantum yield at room temperature because of the non-ideal interface (Fermi-level pinning) and strong electron-phonon coupling in metal (~ 0.1 ps of carrier relaxation time)^{8,4}, posing a big challenge for developing alternative metallic layer. The emerging zero-bandgap graphene can probably improve the junction interface and suppress the device noise due to its ultra-fast electron-electron interaction^{4,8}, improved electron-phonon coupling (~ 1 ps of carrier relaxation time), dangling-bond free surface, and van der Waals contact with semiconductors⁹. However, the high-crystalline graphene, with dominant single-layers, has only 2.3% light absorption, which is too low for mid-infrared photodetection.

Here, we develop a large-area MAG, getting rid of the disadvantages of both single graphene (SLG) or metal, to extend the photodetection wavelength of silicon-based Schottky diode to 10 μm . Fig. 1a-d illustrates the preparation steps of MAG: I) wet-assembly of graphene oxide (GO) nanofilm and chemical reduction^{10,11}, II) borneolum-assisted separation, and III) thermal annealing. The obtained translucent free-standing MAG (diameter of 4.2 cm; thickness of 45 nm, Fig. 1d) owns a high crystallinity with mobility ($\sim 1360 \text{ cm}^2 \text{ V}^{-1} \text{ s}^{-1}$) comparable to that of silicon. The 2D diffraction patterns in the grazing-incidence wide-angle X-ray scattering (GI-WAXS) measurements show all high order hkl reflections of MAG (Fig. 1e), indicating a high graphitization degree with an average interlayer spacing of 3.36 Å. The graphene in MAG has a perfect long-range honeycombed lattice structure without atomic defects founded in a 50 nm-scale (Fig. 1f, g, Supplementary Fig. S2), which is also verified by the undetectable O peak (531.5 eV) (Supplementary Fig. S3) and the ignorable D peak (1343.5 cm^{-1}) (Fig. 1h). In addition, a 1.2° twisted angle of adjacent graphene layers (Fig. 1g) and 4 sets of diffraction spots in a 24-layers MAG (Supplementary Fig. S4a-c) indicate the existence of turbostratic stacking order¹². According to the 2D mode in Fig. 1h, a low fraction ($I(2D_T)/(I(2D_2) + I(2D_T)) \sim 9\%$) of the decoupled structure is detected in MAG¹³, consistent with the lower C mode (42.9 cm^{-1} , ~ 9 -10-layers AB-stacked multilayer graphene stacking with twisted interface) in MAG than that of HOPG (43.4 cm^{-1}) with a similar thickness (25-layers) (Fig. 1h)¹⁴. Notably, the MAG exhibits a

uniform stacking structure. Raman mapping within a 0.01 mm² (400 points, Supplementary Fig. S4e) shows the fractions of AB stacking are all in the range of 90-93%.

The integration of MAG with silicon is compatible with back-end-of-line integration of the complementary-metal-oxide-semiconductor (CMOS) technique. The free-standing MAG was mechanically transferred onto a 2-inch silicon wafer (Fig. 2a, b), forming Schottky heterojunction with van der Waals contact^{9,15}. This clean transfer process avoids possible interface contamination of metallic salts and polymers that are commonly used in the case of single-layer graphene¹⁶. The nano-scale thickness endures MAG high surface energy and thus a good adhesivity, resulting in an atomic-scale contact of MAG with silicon at a 10 μm scale with a low contact resistance of ~ 10⁻⁷ Ω cm⁻² (Fig. 2c, d). Besides, Fig. 2c, d exhibits the highly ordered close-stacked structure and uniform thickness (45 ± 0.5 nm) of MAG, indicating the efficient controllability of our assembly synthesis strategy. Furthermore, the clean transfer method prevents MAG from possibly interface doping and the multilayer stacked bulk structure weakens its surface effect, endowing MAG a thickness-independent intrinsic doping state with a work function of 4.52 ± 0.01 eV (Supplementary Fig. S8 and Tab S1). The uniform structure (thickness and stacking order) and inert doping state of MAG reduce device variation between different pixels and batches, which is a prerequisite for the fabrication of large density pixel array in commercial image sensors.

The high thickness of MAG ensures the MAG/Si an enhanced light absorption. For conventional SLG/Si diodes, the photodetection wavelength is limited in the visible and near-infrared range. In contrast, the MAG, acting as a dominant light-absorbing layer in MAG/Si, extends the absorption bandwidth of silicon-based photodetector to mid-infrared. For instance, the 45 nm-thick MAG shows a flat 80% extinction coefficient (40% absorption and 40% reflection) in 1-10 μm wavelength (Fig. 2d), while SLG only 2.3% absorption as expected (Fig. 2e). The infrared photons absorbed by MAG excite electron-hole pairs, which are separated and transferred from MAG to silicon under a negative bias (Fig. 2b).

The MAG-based junction behaves a more stable normalized noise-spectral-density (NSD) $S(f)/P_{\text{dark}}$ compared with that of SLG. The high thickness of MAG increases the density-of-states in the vicinity of charge-neutrality-point, strengthening the electrical stability of the Fermi level and thus Schottky barrier height (SBH) of MAG/Si. Furthermore, the thick dimension of MAG combined with the clean and atomic-scale interfacial contact with silicon suppresses the carrier

number fluctuation from the surface effect (traps and disorders)¹⁷. Experimental results verify a 2 to 4 orders lower NSD of MAG/Si than that of SLG/Si at bias voltage -1 V to -70 V (Fig. 2f), respectively, which allows a larger signal-to-noise ratio (SNR) for MAG/Si, especially during the avalanche.

Based on the absorption and NSD properties, the SLG/Si device only shows detectable photocurrents at wavelength $\leq 1.5 \mu\text{m}$ (Supplementary Fig. S10c, d). In contrast, the MAG/Si device exhibits distinguishable photoresponse in a wide wavelength range (1-10 μm , Fig. 2g). The enhanced absorption and suppressed noise give rise to 2 to 8 orders increasing of SNR of the MAG/Si compared with that of SLG/Si photodetector (Supplementary Fig. S10c, d).

As a broadband photodetector, the MAG/Si diode exhibits both fast operation speed and high sensitivity. To explore the ultrafast optoelectronic dynamics in MAG/Si, we used the femtosecond (pulse width, $\Delta t = 200\text{fs}$) photoexcitations in MIR¹⁸. A typical external circuit limited response time $\tau_r \sim 120\text{-}130 \text{ ns}$ (4 mm^2 window, Fig. 3a) was obtained at wavelengths of 2 and 4 μm . By reducing the device parasitic capacitance (Supplementary Fig. S13) and resistance in external circuits, a higher speed can be achieved. While at the wavelength of 7 μm , the $\tau_r \sim 300 \text{ ns}$ indicates a different operation mechanism, which will be discussed in the following section. In terms of photoresponse, the MAG/Si exhibits a 10^{11} to 10^6 Jones specific detectivity (D^*) and a 10^{-12} to 10^{-6} $\text{W Hz}^{-0.5}$ noise-equivalent-power (NEP) in the 1-10 μm at room temperature (Fig. 3b), far beyond the detection capabilities of previously reported silicon-based high-speed infrared photodetectors (Extended Data Fig. 1).

The broad photoresponse beyond the intrinsic absorption of silicon in MAG/Si features three distinct working mechanisms (Fig. 3c). The MAG/Si SBH, extracted from the temperature-dependent I - V characteristics (Supplementary Fig. S14d-e), is $\sim 0.3 \text{ eV}$, corresponding to a cutoff wavelength of 2.1 μm (see Supplementary Note 5). For photon energies of $0.5h\nu > \text{SBH}$ (wavelength $< 2.1 \mu\text{m}$), photo-excited electrons directly transport over the barrier and contribute to the photocurrent through the internal photoemission (regime I in Fig. 3c)¹⁹, where the D^* and NEP remain almost constant. When increasing the incident wavelength to 4.6 μm , the energy of direct photo-excited electrons is lower than SBH, so they cannot cross the SBH immediately but thermalize into a Fermi-Dirac distribution in MAG. The thermalized

hot-electrons with energy higher than SBH can emit into silicon afterward (photo-thermionic (PTI) emission, regime II)⁴. In this regime, the portion of hot-electrons with the energy higher than SBH in the Fermi-Dirac distribution drops as the incident photon energy decreases, lowering D^* and increasing NEP greatly (Fig. 3c). In the region of 4.6-10 μm (regime III), negative photocurrents are collected, which possibly results from the screening, photo-gating, and photo-acoustic effects of the massive low energy hot-electrons at the MAG/Si interface²⁰⁻²². Most of the hot-electrons generated in this regime cannot jump over the SBH, resulting in a slight change of photocurrent and thus D^* and NEP as the wavelength increases. The overall three different trends of responsivity (as indicated with circles in Fig. 3d) as a function of incident laser irradiance at different wavelengths also confirm these three dominant electron-transfer mechanisms (Fig. 3d). The cutoff wavelengths of these three regimes can be tuned and the D^* and NEP can be further optimized by tuning the doping state of the silicon (as shown in Supplementary Fig. S10e) or replacing silicon with a semiconductor with higher electron affinity (χ).

According to Fig. 3c, d, we find that the significantly enhanced hot-carrier scattering effect of MAG determines the 2-4 μm MIR detection. The reasons are two-fold. Firstly, MAG has an enhanced light absorption, generating more photo-excited hot-electrons than that of SLG. Secondly, the 45-nm thick cross-section of MAG provides a larger space for hot-electrons to scatter and multiply. At the moderate electric field ($\sim 10^3 \text{ V cm}^{-1}$), a large number of hot-electrons in MAG transport towards the MAG/Si interface facilitated by the AB-stacking dominant structure: (1) the prolonged hot-carrier lifetime and thus the long out-of-plane hot-carrier diffusion length²³, (2) the relaxed conservation of in-plane momentum from carrier scattering²⁴, and (3) the finite out-of-plane velocity (v_z) from the momentum uncertainty due to the presence of a few misorientations in the stacking order (Fig. 1f). The synergistic combination of the effects (2-3) enhances the wave-like over particle nature of electrons until they completely transfer into silicon with a definite momentum, increasing the hot-electron density overcoming the MAG/Si barrier. Hence, the charge transfer efficiency mainly depends on the out-of-plane hot-electron diffusion length (out-of-plane velocity multiplies relaxation time). Moreover, in SLG/Si case, based on the simplified Vickers-Mooney model, only a portion of hot-electrons with energy and momentum falling within the escape cone is transferred into silicon, and the rest scatter back to SLG²⁵. In

comparison, in the MAG/Si case, some of the backscattered hot-electrons are expected to be redirected into the escape cone through phonon and interface wall scattering due to the large available cross-section of MAG (Fig. 3c, regime II). Therefore, the trade-off between out-of-plane charge transfer and the recombination in MAG achieves the maximum quantum efficiency (QE) at 45 nm in our case (Fig. 3e).

To further investigate the hot-carrier dynamics in MAG/Si, we conducted a pump-probe transient absorption measurement (Supplementary Fig. S16) on our detectors. The pump laser wavelength is 3.5 μm , with the probe from 1.2-1.6 μm , which is just above the SBH. When pump laser fluences is $> 1 \text{ mW mm}^{-2}$, the scattered electron occupation close to the charge neutrality point (0.37-0.42 eV, Fig. 4a) and the upshift of a fraction of hot-electrons to the energies comparable to SBH ($E > h\nu_{\text{pump}}$) are clear indications of Auger recombination (AR)²⁶. In this fluence regime, the combination of impact excitation dominated in the initial tens of femtoseconds and AR prevailed subsequently result in a large pool of hot-electrons with energies near SBH ($E \approx \phi_B$) (Fig. 4a). The AR process dominates carrier kinetics in MAG until it reaches the optical phonon bottleneck ($\sim 200 \text{ meV}$) at $\sim 1 \text{ ps}$, and then the relaxation occurs via an interaction with acoustic phonons within $\sim 23 \text{ ps}$ as displayed in Fig. 4b. Due to the thick crystalline MAG and non-polar property of silicon, the cooling from disorder and substrate-based surface plasmon polariton is weak in our devices²⁷. The dominant carrier relaxation mechanism gradually shifts from AR to acoustic phonon emission at longer wavelengths, which is further confirmed from the elimination of the fast component (within 1.5 ps) in the bi-exponential fitting results (Fig. 4b). The out-of-plane hot-electron diffusion coefficient and cooling time are about $1 \text{ cm}^2 \text{ s}^{-1}$ and 23 ps, respectively. From the saturation absorption and power dependent analysis, the two-photon or multi-photon absorption from either MAG or silicon is ruled out in our case (Supplementary Fig. S17). By extracting the number of hot-electrons $n(E)$ from transient absorption ΔA and the current collected from silicon, the hot-electron transfer efficiency η_e (3.5 μm) between MAG and silicon is obtained on the order of 10^{-3} - 10^{-5} under the irradiance from 10 to 100 mW mm^{-2} . We also quantified the hot-electron scattering effect by calculating the hot-carrier-multiplication. The density of hot-electrons with higher energy than chemical potential exceeds that in the conduction band immediately after photo-excitation with a peak multiplication value ~ 20 (1 mW mm^{-2}) at 700 fs (Fig. 4c).

At the high electric field regime ($\sim 10^5$ V cm⁻¹), a ~ 5 μm depleted region in silicon is induced, generating additional electron-hole pairs through impact ionization. The current amplification gain due to the avalanche in silicon reaches 10^2 as the bias V_b increases up to -70 V for all laser irradiance (Fig. 4d) with an excess noise factor of 10 (Supplementary Note 4). The increased NSD (Fig. 2f) with the bias also indicates the avalanche in silicon²⁸. The drastic increase at -30 V indicates the beginning of the avalanche (Supplementary Fig. S19). Combining the carrier-carrier scattering in MAG and carrier multiplication through the avalanche in silicon, the MAG/Si shows an external QE of 0.1-10 % at 3.5 μm under the irradiance from 10 to 100 mW mm⁻² (Fig. 4e).

MAG is a promising candidate for CMOS technology due to its robust mechanical property, uniform structure, and low cost. As shown in Fig. 5a, MAG was etched into a neat array composed of 50 μm -scale pixels by standard lithography and oxygen plasma^{29,30}. Combined with CMOS-compatible process flow, MAG/Si was packed into a 9×9 pixel array image sensor (Fig. 5b, c). The D^* variation among each pixel was tested less than one order (Fig. 3b) because of the uniformity of MAG in thickness and stacking order. Fig. 5d presents the room-temperature images captured by the MAG/Si with a mask of the Chinese character “杭 (Hang)” at the wavelengths 1.55 μm , 3 μm , and 10 μm . The array-level CMOS compatibility of wafer-scale MAG offers opportunities to develop room-temperature silicon image sensors at broad infrared frequencies that conventional Schottky diodes are not readily applicable.

This work demonstrates a high-performance MAG/Si Schottky diode with fast response time, low NSD, and record response wavelength, far beyond state-of-the-art silicon-based high-speed infrared photodetectors. Such outstanding detection capability is achieved by introducing high crystalline MAG that compatible well with CMOS technology as an absorption layer, which is integrated with silicon with a clean and atomic-scale contact interface. This work opens a new avenue from macroscopic defective GO to high-performance optoelectronic devices, provides a strategy to explore hot-carrier dynamics in highly stacked two-dimensional systems, and demonstrates a feasible way to develop low-cost and large-scale broadband graphene-based photodetectors for CMOS image sensors at room temperature.

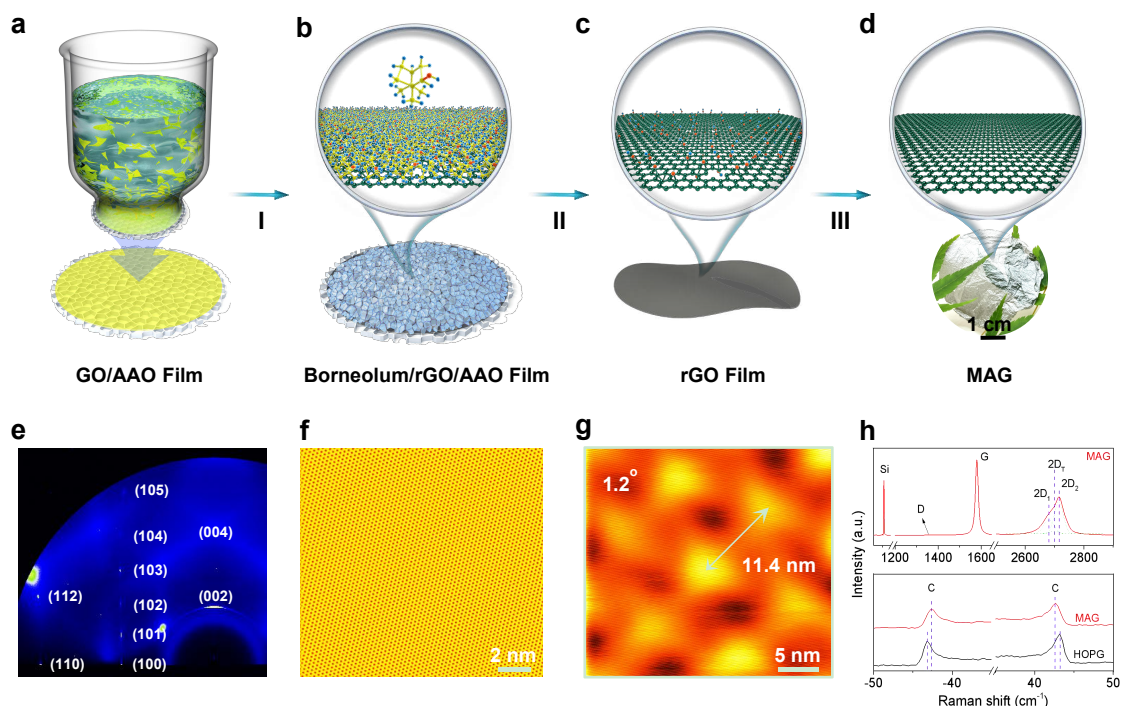


Fig. 1 | Preparation and structural characterization of MAG. **a-d**, Schematic illustration of the preparation of free-standing MAG (see Methods and Supplementary Fig. S1 for more details). First, a diluted GO solution is filtrated under vacuum with anodic aluminum oxide (AAO) filters; then the GO/AAO membrane is reduced by HI vapor (Step I) and separated by the contraction effect of hot polycrystalline borneolum (Step II); after a low-temperature (60 °C) borneolum sublimation and high-temperature (2800 °C) treatment (Step III) to remove borneolum and defects, free-standing GO-based MAG with a diameter of 4.2 cm is obtained. Note: Yellow and red balls in models represent oxygen and hydrogen elements, respectively. To enhance the contrast, the carbon element in models of borneolum (yellow ball) and GO (green ball) are shown in yellow and green, respectively. The image in **d** (down) shows the translucent and free-standing MAG. **e**, The synchrotron GIWAXS 2D patterns of MAG (thickness of 45 nm) on a silicon substrate. **f-g**, The scanning-tunneling-microscopy (STM) topographic images of MAG, showing perfect hexagonal lattice structure (**f**) and regular moiré pattern with a twisted angle of $\theta \approx 1.2^\circ$ (**g**). **h**, Raman spectra of MAG on the silicon substrate. The 2D peak is fitted with 3 Lorentzian peaks: $2D_1$ ($\sim 2680 \text{ cm}^{-1}$) and $2D_2$ ($\sim 2720 \text{ cm}^{-1}$) for AB stacked graphite and $2D_T$ ($\sim 2700 \text{ cm}^{-1}$) for turbostratic graphite (see Supplementary Fig. S4d).

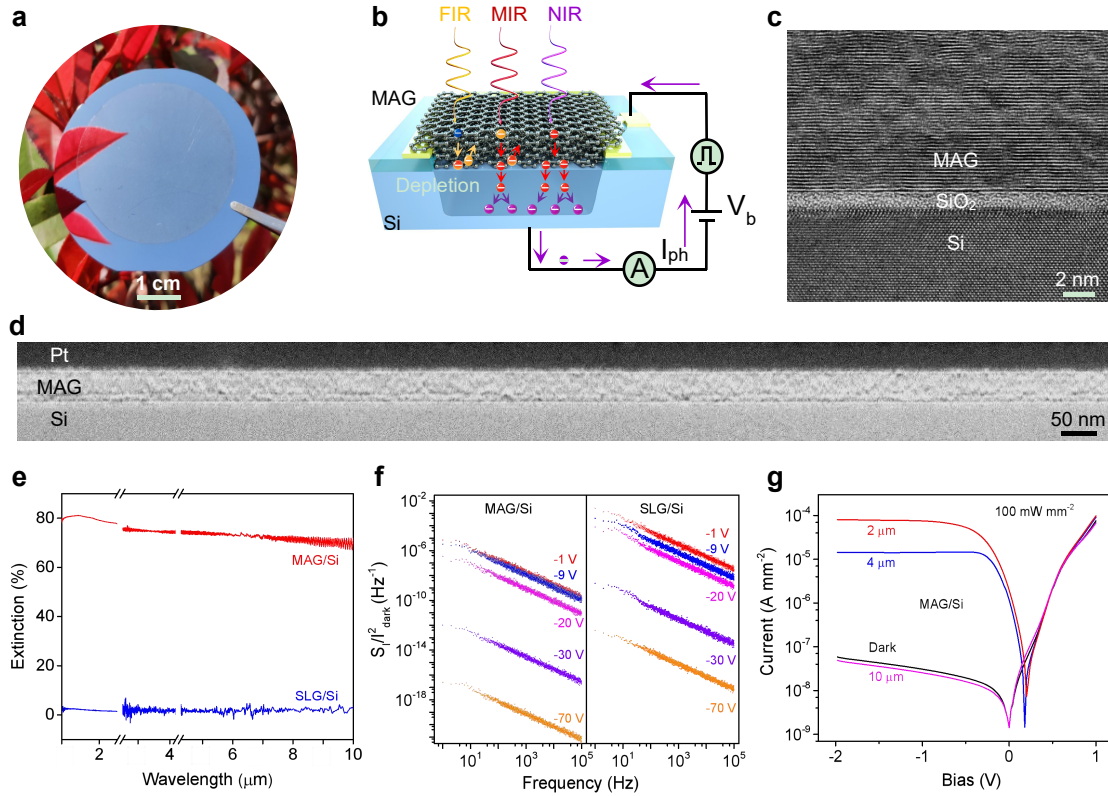


Fig. 2 | Device structural characterization of MAG/Si. **a**, A photo of MAG transferred on a 2-inch silicon wafer (see Supplementary Fig. S5). **b**, A schematic of the MAG/Si device shows the charge transport and current flow. **c**, HR-TEM image of the MAG/Si showing an atomic-scale contacting interface (see Supplementary Fig. S6). The highly aligned (002) lattice fringes and corresponding sharp discrete spots in the fast-Fourier-transform (FFT) pattern indicate a highly ordered structure of MAG with the interlayer space of $3.36 \pm 0.04 \text{ \AA}$, consistent with the result of GI-WAXS. **d**, Cross-sectional TEM image of MAG/Si with Pt layer on the top for protection during focused-ion-beam (FIB) milling (see Supplementary Fig. S7). **e**, The Fourier-transform-infrared-spectroscopy (FTIR) extinction spectra ($1-T/T_0$) of SLG/Si and MAG/Si from 1 to 10 μm , where T is the transmission through MAG/Si and SLG/Si, and T_0 is the transmission only through Si substrate underneath (see Supplementary Fig. S9). **f**, The NSD $S(f)/P_{\text{dark}}$ as a function of frequency at a different reverse bias of MAG/Si (see Supplementary Fig. S10a, b). The window size is $2 \text{ mm} \times 2 \text{ mm}$. **g**, The direct-current I - V curves of MAG/Si under dark, and laser illumination at 2 μm , 4 μm , and 10 μm wavelength with 200 fs pulse width, 100 kHz repetition rate and 50 mW mm^{-2} irradiances. All the scanned I - V curves showed negligible hysteresis indicating a clean MAG/Si interface.

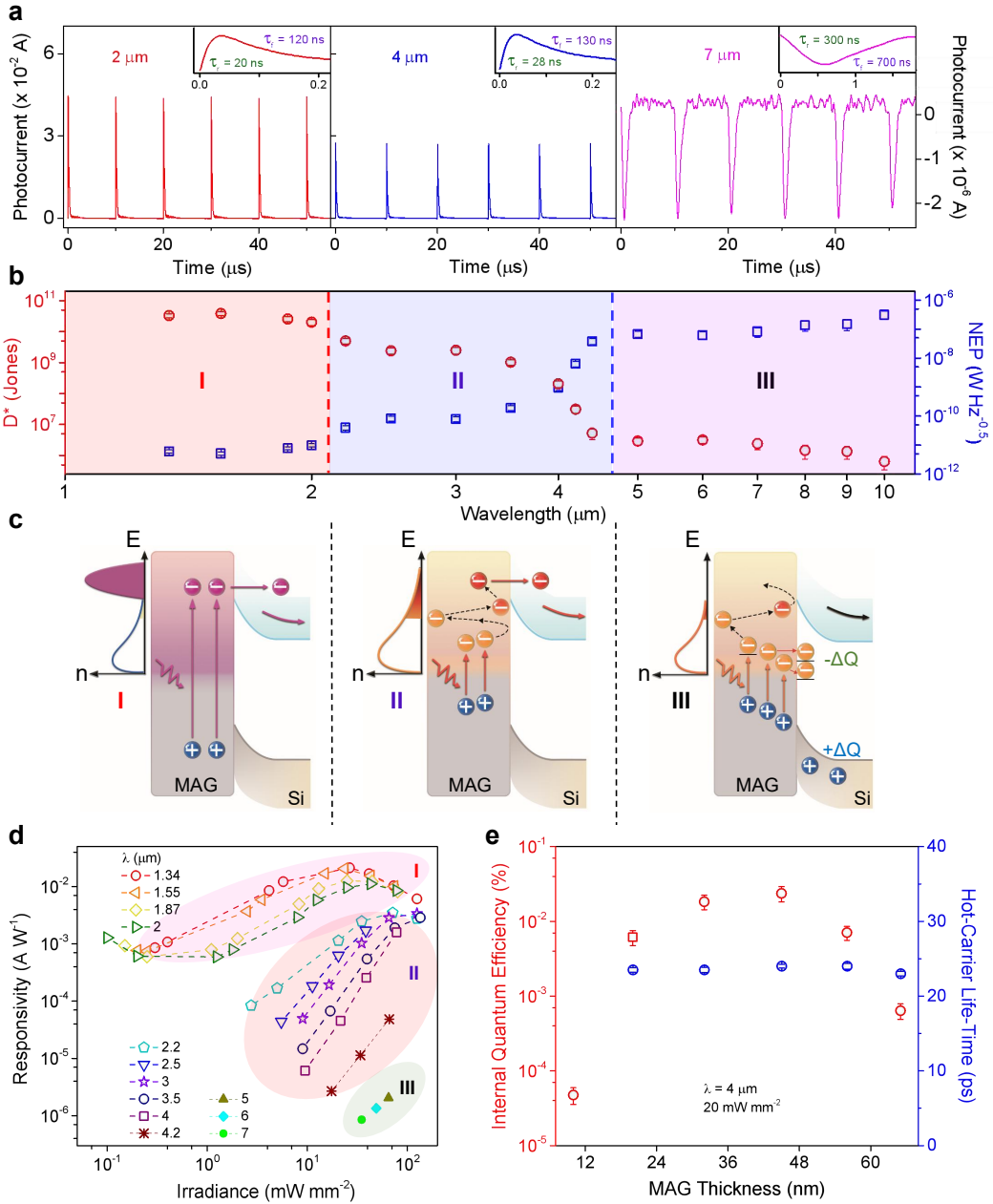


Fig. 3 | Transient photoresponse of MAG/Si. **a**, The photocurrent of MAG/Si in time domain under pulsed-laser (200 fs of pulse width, 100 kHz of repetition rate) illumination at 2 μm , 4 μm , and 7 μm wavelength with a 50 mW mm^{-2} irradiance. The photocurrent in the vertical axis at 4 μm is on the same scale as at 2 μm on the left (see Supplementary Fig. S11, 12, Video S1). Insets show the corresponding single periods. **b**, The D^* and NEP of MAG/Si as a function of laser wavelength under a fixed irradiance of 10 mW mm^{-2} (see Supplementary Fig. S14a-c). **c**, the corresponding energy-band diagrams for operation mechanism at the three wavelengths above. **d**, The responsivity of MAG/Si as a function of laser irradiance at different wavelengths. **e**, The internal-QE and hot-carrier life-time of MAG/Si as a function of MAG thickness at 4 μm laser wavelength with a fixed irradiance of 20 mW mm^{-2} (see Supplementary Fig. S15).

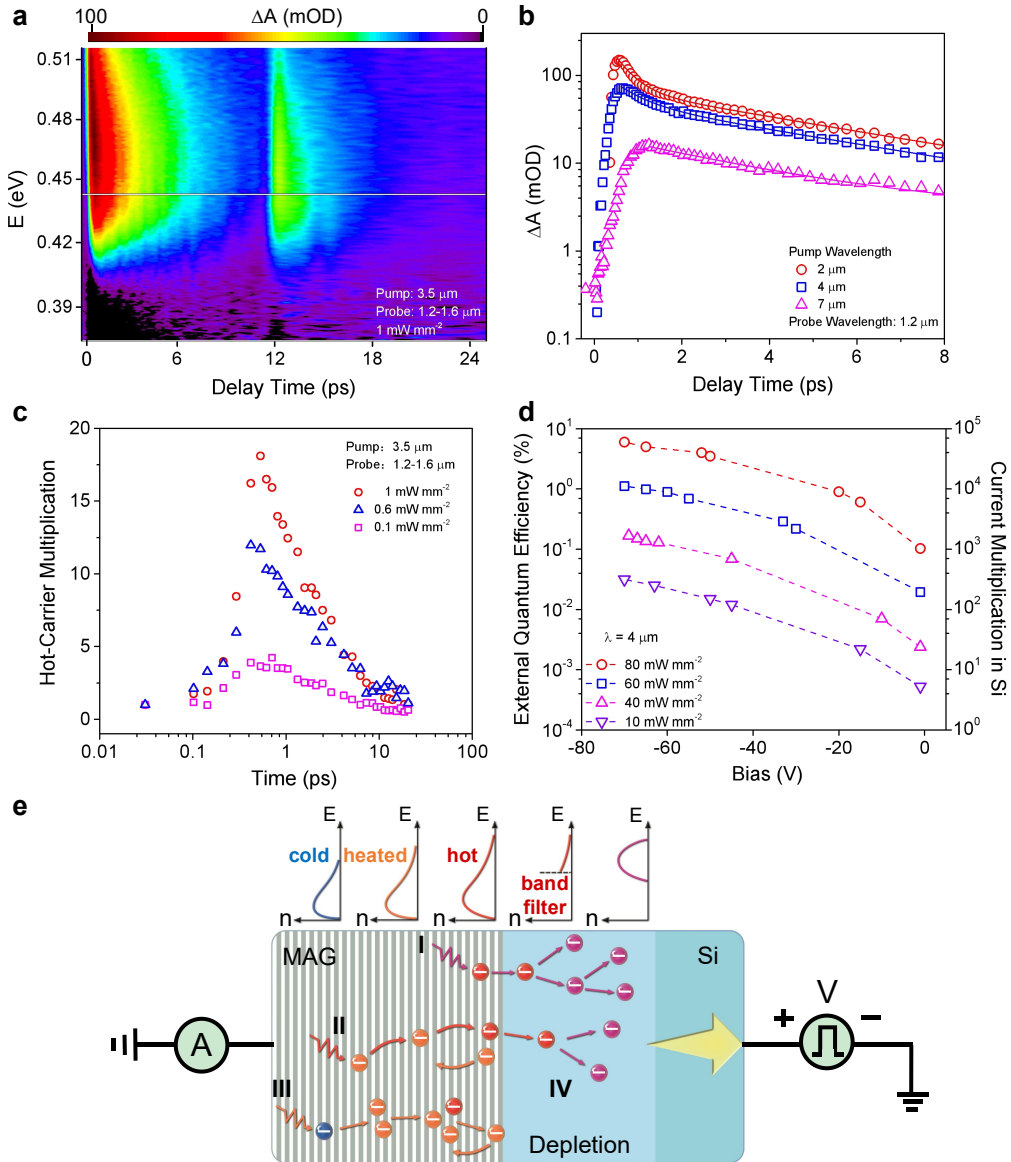


Fig. 4 | Hot-carrier transport in MAG/Si. **a**, 2D transient absorption map of MAG/Si as functions of delay time and the half of incident photon energy (the mOD means milli-optical density). The sample is pumped at 3.5 μm with an irradiance of 1 mW mm^{-2} . The second peak at ~ 10 ps is due to photo-excitation from the reflected pump laser on the silicon substrate (thickness of 500 μm) underneath. **b**, The transient-absorption kinetics probed at 1.2 μm with a pump at 2 μm , 4 μm , and 7 μm (see Supplementary Fig. S18). **c**, The hot-carrier multiplication factor as a function of time under different pump irradiance at 3.5 μm and probed in the range from 1.2 to 1.6 μm . **d**, The external-QE and current amplification factor as a function of bias V_b of MAG/Si under 4 μm wavelength laser with different irradiance (see Supplementary Fig. S19, Video S2). **e**, The operation mechanism schematic of MAG/Si photodiode under 2 μm (I), 4 μm (II), and 7 μm (III) photo-excitations and avalanche (IV).

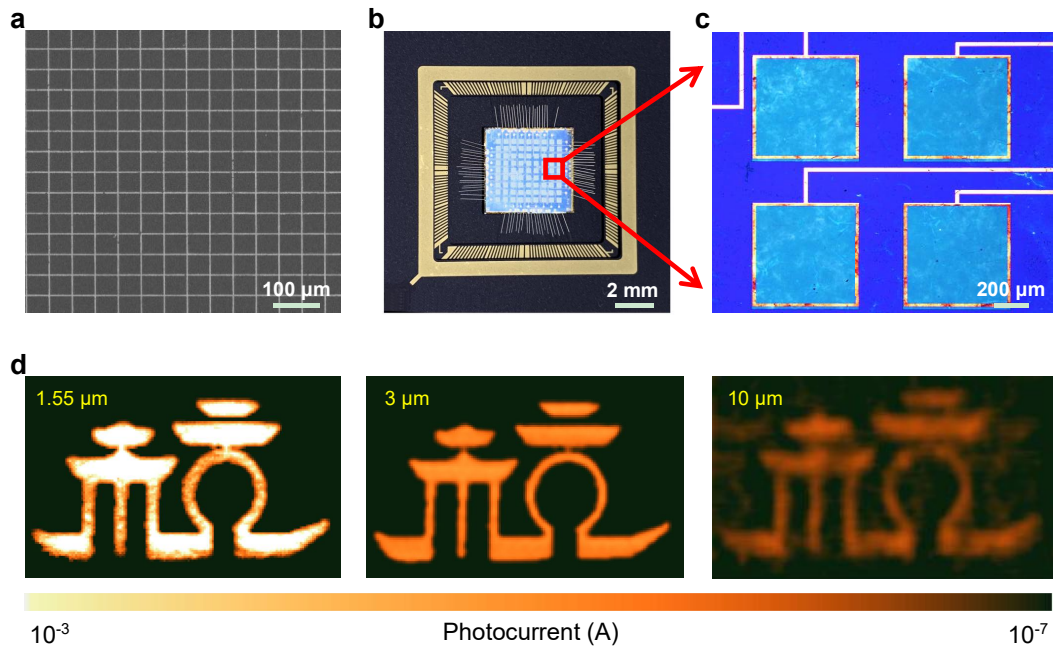


Fig. 5 | MAG/Si image sensors. **a**, A SEM image shows the plasma etched MAG pixel array on silicon with a dimension of $50\ \mu\text{m} \times 50\ \mu\text{m}$ for each pixel (see Supplementary Fig. S20). **b-c**, A photo of 9×9 packed MAG/Si image sensor with the zoomed-in optical image. **d**, The scanned images of a Chinese character “杭 (Hang)” representing the Hangzhou city at $1.55\ \mu\text{m}$, $3\ \mu\text{m}$, and $10\ \mu\text{m}$ laser wavelength (see Supplementary Fig. S21). The color bar represents the photocurrent level.

- 1 Neto, A. H., Guinea, F., Peres, N. M., Novoselov, K. S. & Geim, A. K. The electronic properties of graphene. *Rev. Mod. Phys.* **81**, 109-162 (2009).
- 2 Bonaccorso, F., Sun, Z., Hasan, T. & Ferrari, A. C. Graphene photonics and optoelectronics. *Nat. Photonics* **4**, 611-622 (2010).
- 3 Nair, R. *et al.* Fine structure constant defines visual transparency of graphene. *Science* **320**, 1308-1308 (2008).
- 4 Massicotte, M. *et al.* Photo-thermionic effect in vertical graphene heterostructures. *Nat. Commun.* **7**, 12174 (2016).
- 5 Mihnev, M. T. *et al.* Electronic cooling via interlayer Coulomb coupling in multilayer epitaxial graphene. *Nat. Commun.* **6**, 8105 (2015).
- 6 Sharma, B. L. Metal-semiconductor Schottky barrier junctions and their applications. *Springer Science & Business Media* **11** (2013).
- 7 Bartolomeo, A. D. Graphene Schottky diodes: an experimental review of the rectifying graphene/semiconductor heterojunction. *Phys. Rep.* 1-58 (2016).
- 8 Balandin, A. A. Low-frequency $1/f$ noise in graphene devices. *Nat. Nanotechnol.* **8**, 549-555 (2013).
- 9 Liu, Y. *et al.* Approaching the Schottky-Mott limit in van der Waals metal-semiconductor junctions. *Nature* **557**, 696-700 (2018).
- 10 Dikin, D. A. *et al.* Preparation and characterization of graphene oxide paper. *Nature* **448**, 457-460 (2007).
- 11 Pei, S. & Cheng, H. M. The reduction of graphene oxide. *Carbon* **50**, 3210-3228 (2012).
- 12 Bistritzer, R. & Macdonald, A. H. Moiré bands in twisted double-layer graphene. *Proc. Natl. Acad. Sci.* **108**, 12233-12237 (2011).
- 13 Cançado, L. G. *et al.* Measuring the degree of stacking order in graphite by Raman spectroscopy. *Carbon* **46**, 272-275 (2008).
- 14 Wu, J.-B. *et al.* Resonant Raman spectroscopy of twisted multilayer graphene. *Nat. Commun.* **5**, 5309 (2014).
- 15 Bae, S. *et al.* Integration of bulk materials with two-dimensional materials for physical coupling and applications. *Nat. Mater.* **18**, 550-560 (2019).
- 16 Gao, L. *et al.* Face-to-face transfer of wafer-scale graphene films. *Nature* **505**, 190-194 (2014).
- 17 Liu, G., Rumyantsev, S., Shur, M. S. & Balandin, A. A. Origin of $1/f$ noise in graphene multilayers: Surface vs. volume. *Appl. Phys. Lett.* **102**, 093111 (2013).
- 18 Massicotte, M. *et al.* Picosecond photoresponse in van der Waals heterostructures. *Nat. Nanotechnol.* **11**, 42-46 (2016).
- 19 Casalino, M. Internal photoemission theory: comments and theoretical limitations on the performance of near-infrared silicon Schottky photodetectors. *IEEE J. Quantum Electron.* **52**, 1-10 (2016).
- 20 Tomadin, A. *et al.* The ultrafast dynamics and conductivity of photoexcited graphene at different Fermi energies. *Sci. Adv.* **4**, 5313 (2018).
- 21 Fang, H. & Hu, W. Photogating in low dimensional photodetectors. *Adv. Sci.* **4**, 1700323 (2017).
- 22 Liu, J. *et al.* Semimetals for high-performance photodetection. *Nat. Mater.* **19**, 830-837 (2020)
- 23 Stange, A. *et al.* hot-electron cooling in graphite: Supercollision versus hot phonon decay. *Phys. Rev. B* **92**, 184303 (2015).
- 24 Ang, Y. S., Yang, H. Y. & Ang, L. K. Universal scaling laws in Schottky heterostructures based on two-dimensional materials. *Phys. Rev. Lett.* **121**, 056802 (2018).

- 25 Kimata, M., Denda, M., Iwade, S., Yutani, N. & Tsubouchi, N. A wide spectral band photodetector with PtSi/p-Si Schottky-barrier. *Int. J. Infrared Millimeter Waves* **6**, 1031-1041 (1985).
- 26 Winzer, T., Jago, R. & Malic, E. Experimentally accessible signatures of Auger scattering in graphene. *Phys. Rev. B* **94**, 235430 (2016).
- 27 Graham, M. W., Shi, S.-F., Ralph, D. C., Park, J. & McEuen, P. L. Photocurrent measurements of supercollision cooling in graphene. *Nat. Phys.* **9**, 103-108 (2013).
- 28 Kanbe, H., Kimura, T., Mizushima, Y. & Kajiyama, K. Silicon avalanche photodiodes with low multiplication noise and high-speed response. *IEEE Trans. Electron Devices* **23**, 1337-1343 (1976).
- 29 Goossens, S. *et al.* Broadband image sensor array based on graphene-CMOS integration. *Nat. Photonics* **11**, 366-371 (2017).
- 30 Akinwande, D. *et al.* Graphene and two-dimensional materials for silicon technology. *Nature* **573**, 507-518 (2019).

Methods

Preparation of MAG. MAG was prepared from defective GO with an average size of $100 \mu\text{m}^3$, provided by Hangzhou Gaoxi Technology Co., Ltd. (<http://www.gaoxitech.com>). First, a diluted GO solution with a concentration of $4 \mu\text{g L}^{-1}$ was filtrated under vacuum by AAO filters (Whatman, pore size, $0.2 \mu\text{m}$; diameter, 48 mm). The supported GO membrane on the AAO filter was then reduced by HI vapor for 4 hours in a sealed container heated under $100 \text{ }^\circ\text{C}$. Then the rGO/AAO membrane was placed on a bottle (diameter, 48 mm) containing borneolum with the GO side facing borneolum. The bottle was then heated to $120 \text{ }^\circ\text{C}$ to deposit borneolum (10-50 mg) on the surface of the rGO film. Three to ten minutes later, the borneolum/rGO/AAO membrane was slowly cooled to room temperature, and the borneolum/rGO film automatically separated from the AAO membrane. Subsequently, a continuous heating process ($60 \text{ }^\circ\text{C}$) was used to remove borneolum, leaving a freestanding rGO film. Finally, the freestanding rGO film was further heated at $2800 \text{ }^\circ\text{C}$ (heating rate of $20 \text{ }^\circ\text{C}/\text{min}$) for 1 hour to heal defects in high-temperature graphite furnace (NTG-SML-50L, Changsha Nuotian Electronic Technology) protected by Ar_2 .

Material characterizations. Raman spectra were measured in back-scattering at room temperature with a Jobin-Yvon HR800 Raman system, equipped with a liquid-nitrogen-cooled CCD, an x 100 objective lens (numerical aperture ~ 0.90), and several gratings. The excitation wavelength was 633 nm from a He-Ne laser. Plasma lines were removed from the laser signals, using BragGrate Bandpass filters. Measurements down to 5 cm^{-1} for each excitation were enabled by three BragGrate notch filters with optical density 3 and FWHM = $5\text{-}10 \text{ cm}^{-1}$. The typical laser power is $\sim 1 \text{ mW}$ to avoid sample heating. TEM images were acquired on a Hitachi H-9500

instrument operating at 300 kV. XPS was performed with a PHI 5000C ESCA System operated at 14.0 kV and all binding energies were referenced to the C 1s neutral carbon peak at 284.6 eV. The absorption spectra were obtained by an FT-IR Spectrometer (Nicolet iN10, Thermofisher Scientific) with a detecting diameter of 300 μm . The STM experiments were performed with an ultrahigh vacuum (UHV) and a low-temperature (~ 77 K) STM system (UNISOKU USM-1500S). The samples were cleaved in the UHV chamber and immediately inserted into the measurement stage. The STM topography was conducted at a sample bias $V = -100$ mV and a setpoint current $I = 200$ pA. The electron mobility was measured with a Hall Effect Measurement System (Lakeshore 7604). The Grazing Incidence Wide Angle X-ray Scattering measurements were performed at the 14b beamline of the Shanghai Synchrotron Radiation Facility in Shanghai, Republic of China. The energy of the X-rays was 18.981 keV and the wavelength was 0.653 \AA . Thin-film samples were transferred to silicon wafer substrates for measurement.

Device fabrication. The device was fabricated on a lightly-doped n-type silicon wafer with a 100 nm SiO_2 layer. (1) The SiO_2 layer was patterned by photolithography first. Then the e-beam deposition and thermal evaporation (Angstrom Engineering) were used to deposit Cr/Au (5/100 nm) as top electrodes. (2) After lift-off, photolithography was conducted again to pattern silicon windows with a size of 2 mm \times 2 mm. SiO_2 in the window was subsequently etched away with a buffered oxide etchant. The backside oxide of the silicon wafer was also etched simultaneously during this process. (3) The MAG was then transferred onto the etched silicon window. The gap between MAG and silicon was filled with water to remove the wrinkles. The surface of MAG was then purged with nitrogen before the ethanol was completely volatilized. (4) The device was further patterned by photolithography to etch the MAG outside the Cr/Au top electrode by oxygen plasma. (5) Finally, Ohmic contact is formed between the back-side of silicon and copper tape. Au wires were then bonded with the top and back electrodes.

Device characterization. The I - V curves were collected from Keithley Semiconductor Analyzer 2400. The device and the trans-impedance amplifier (DHPCA-100, FEMTO, 200 MHz bandwidth) were connected with an oscilloscope (Keysight DSO 9404A, 4 GHz bandwidth) to measure the photo-voltages. Periodic pulse lasers (Light Conversion, OPA-Series, 1 μm to 10 μm , 200 fs pulse width, and 100 kHz repetition rate) were used as the light source. The noise spectra were recorded by a noise measurement system (PDA NC300L, 100 kHz bandwidth). Infrared bandpass filters

(FB2000-500 to FB4000-500, Thorlabs) were used to filter out the stray light from the MIR laser. A calcium fluoride aspherical lens system was used to focus the infrared light on the device. The power was measured by a thermopile detector (Newport 1918-R). For the photograph, we built a scanning system with a focused laser and programmable X-Y stage. A data acquisition (DAQ) card was used to obtain the photocurrent data.

Ultrafast transient absorption spectroscopy measurement. The femtosecond transient absorption setup used for this study was based on a PHAROS laser system (Light Conversion, 1030 nm, < 190 fs, 200 uJ per pulse, and 100 kHz repetition rate), nonlinear frequency mixing techniques, and the Femto-TA100 spectrometer (Time-Tech Spectra). Briefly, the 1030 nm output pulse from the regenerative amplifier was split into two parts with an 80 % beam splitter. The reflected part was used to pump an ORPHEUS Optical Parametric Amplifier (OPA) which generates a wavelength-tunable laser pulse from 300 nm to 15 μm . The transmitted 1030 nm beam was split again into two parts. One part with less than 50 % was attenuated with a neutral density filter and focused into a YAG window to generate a white light continuum (WLC) from 500 nm to 1600 nm used for probe beam. The probe beam was focused with an Ag parabolic reflector onto the sample. After the sample, the probe beam was collimated and then focused on a fiber-coupled spectrometer with CMOS sensors and detected at a frequency of 10 kHz. The intensity of the pump pulse used in the experiment was controlled by a variable neutral-density filter wheel. The delay between the pump and probe pulses was controlled by a motorized delay stage. The pump pulses were chopped by a synchronized chopper at 5 kHz and the absorbance change was calculated with two adjacent probe pulses (pump-blocked and pump-unblocked). All experiments were performed at room temperature.

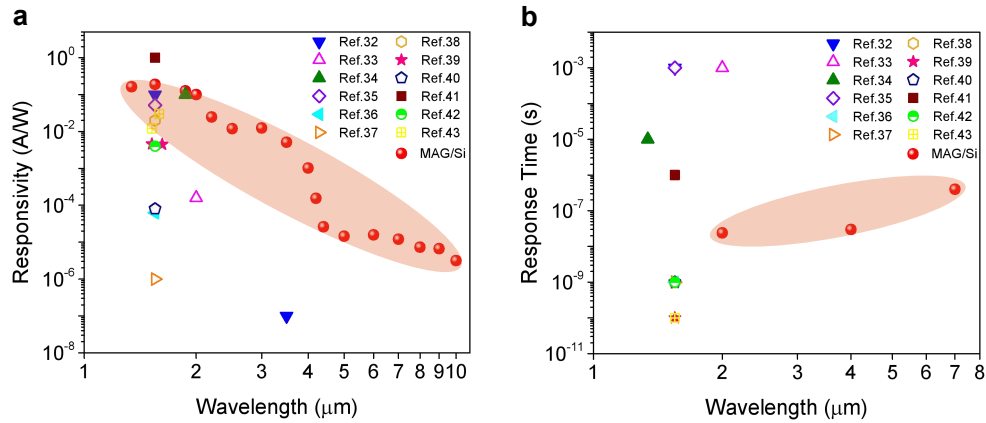
Acknowledgements

The authors would like to thank Prof. Tony Low for helpful discussions and comments. This work was supported by the National Natural Science Foundation of China (Nos. 51803177, 51533008, 51703194, 51603183, 21325417, 21805242, 61674127, 61874094, and 61704150), National Key R&D Program of China (No. 2016YFA0200200), ZJ-NSF (LZ17F040001), China Postdoctoral Science Foundation (2019M652081), Hundred Talents Program of Zhejiang University (188020*194231701/113), Key research and development plan of Zhejiang Province

(2018C01049), and the Fundamental Research Funds for the Central Universities (No. 2017QNA4036, 2017XZZX001-04, 2017XZZX008-06, 2016XZZX001-05).

Author Contributions Y. X. and C. G. conceived the project. L. P., S. D., L. L., S. C. B., Y. X. and C. G. designed the experiment. W. F., X. C., L. L., X. L., R. L., J. L., and W. Y. assisted in part of the experiment. L. P., S. D., L. L., Y. X. and C. G plotted the figures and wrote the manuscript. All authors contributed to the discussion and analysis of the results.

Competing interests The authors declare no competing interests.



Extended Data Fig. 1 | Comparison of state-of-the-art graphene-silicon infrared photodetectors at room temperature (see Supplementary Table S2).

- 31 Dong, L., Yang, J., Chhowalla, M. & Loh, K. P. Synthesis and reduction of large sized graphene oxide sheets. *Chem. Soc. Rev.* **46**, 7306-7316 (2017).
- 32 Liu, X. *et al.* Infrared photodetector based on the photothermionic effect of graphene-nanowall/silicon heterojunction. *ACS Appl. Mater. Interfaces* **11**, 17663-17669 (2019).
- 33 Casalino, M. *et al.* Free-space Schottky graphene/silicon photodetectors operating at 2 μm. *ACS Photonics* **5**, 4577-4585 (2018).
- 34 Du, S. *et al.* Graphene/silicon-quantum-dots/Si Schottky-pn cascade heterojunction for short-wavelength infrared photodetection. *IEEE International Electron Devices Meeting (IEDM)* 8.7.1-8.7.4 (2017).
- 35 Li, J. *et al.* Direct integration of polycrystalline graphene on silicon as a photodetector via plasma-assisted chemical vapor deposition. *J. Mater. Chem. C* **6**, 9682-9690 (2018).
- 36 Casalino, M., Coppola, G., Iodice, M., Rendina, I. & Sirleto, L. Critically coupled silicon Fabry-Perot photodetectors based on the internal photoemission effect at 1550 nm. *Opt. Express* **20**, 12599-12609 (2012).
- 37 Casalino, M. *et al.* Cavity enhanced internal photoemission effect in silicon photodiode for sub-bandgap detection. *J. Lightwave Technol.* **28**, 3266-3272 (2010).
- 38 Casalino, M. *et al.* Vertically illuminated, resonant cavity enhanced, graphene-silicon Schottky photodetectors. *ACS Nano* **11**, 10955-10963 (2017).
- 39 Zhu, S., Yu, M. B., Lo, G. Q. & Kwong, D. L. Near-infrared waveguide-based nickel silicide Schottky-barrier photodetector for optical communications. *Appl. Phys. Lett.* **92**, 081103 (2008).
- 40 Casalino, M. *et al.* Cu/p-Si Schottky barrier-based near infrared photodetector integrated with a silicon-on-insulator waveguide. *Appl. Phys. Lett.* **96**, 241112 (2010).
- 41 Chen, Z. *et al.* Synergistic effects of plasmonics and electron trapping in graphene short-wave infrared photodetectors with ultrahigh responsivity. *ACS Nano* **11**, 430-437 (2017).
- 42 Casalino, M., Iodice, M., Sirleto, L., Rendina, I. & Coppola, G. Asymmetric MSM sub-bandgap all-silicon photodetector with low dark current. *Opt. Express* **21**, 28072-28082 (2013).
- 43 Zhu, S., Chu, H. S., Lo, G. Q., Bai, P. & Kwong, D. L. Waveguide-integrated near-infrared detector with self-assembled metal silicide nanoparticles embedded in a silicon p-n junction. *Appl. Phys. Lett.* **100**, 061109 (2012).

Figures

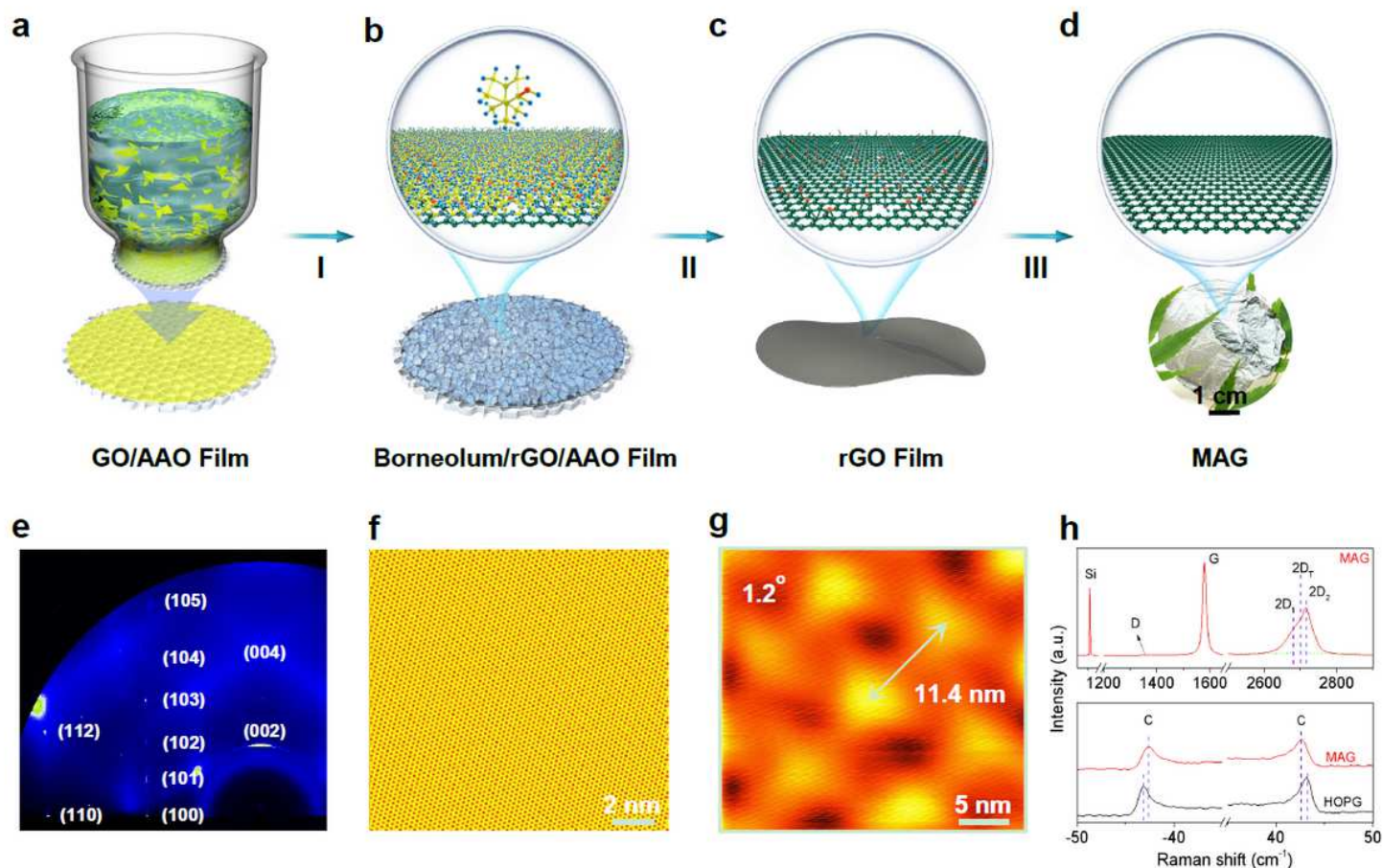


Figure 1

Preparation and structural characterization of MAG. a-d, Schematic illustration of the preparation of free-standing MAG (see Methods and Supplementary Fig. S1 for more details). First, a diluted GO solution is filtrated under vacuum with anodic aluminum oxide (AAO) filters; then the GO/AAO membrane is reduced by HI vapor (Step I) and separated by the contraction effect of hot polycrystalline borneolum (Step II); after a low-temperature (60 oC) borneolum sublimation and high-temperature (2800 oC) treatment (Step III) to remove borneolum and defects, free-standing GO-based MAG with a diameter of 4.2 cm is obtained. Note: Yellow and red balls in models represent oxygen and hydrogen elements, respectively. To enhance the contrast, the carbon element in models of borneolum (yellow ball) and GO (green ball) are shown in yellow and green, respectively. The image in d (down) shows the translucent and free-standing MAG. e, The synchrotron GIWAXS 2D patterns of MAG (thickness of 45 nm) on a silicon substrate. f-g, The scanning-tunneling-microscopy (STM) topographic images of MAG, showing perfect hexagonal lattice structure (f) and regular moiré pattern with a twisted angle of $\theta \approx 1.2^\circ$ (g). h, Raman spectra of MAG on the silicon substrate. The 2D peak is fitted with 3 Lorentzian peaks: 2D₁ (~2680 cm⁻¹) and 2D₂ (~2720 cm⁻¹) for AB stacked graphite and 2D_T (~2700 cm⁻¹) for turbostratic graphite (see Supplementary Fig. S4d).

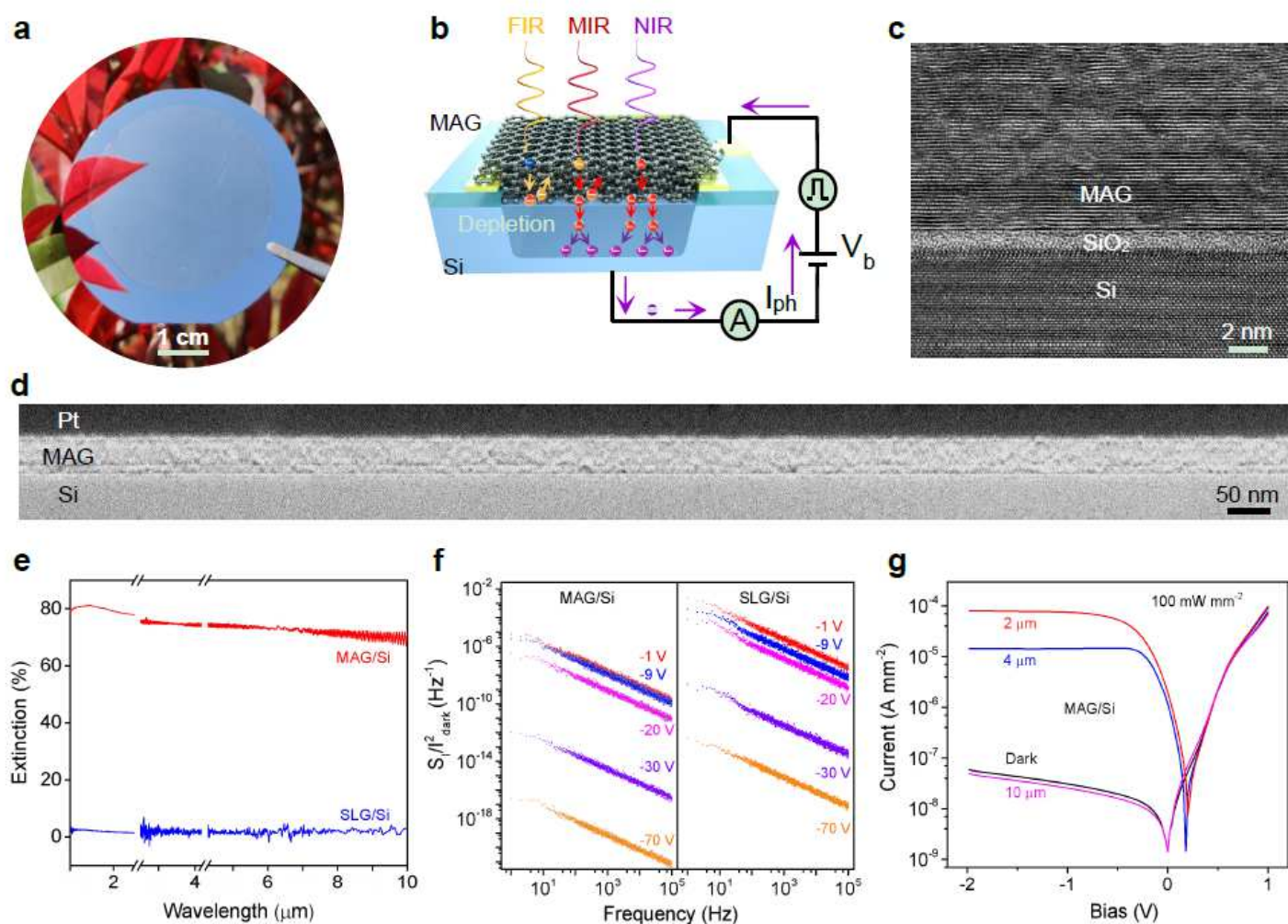


Figure 2

Device structural characterization of MAG/Si. a, A photo of MAG transferred on a 2-inch silicon wafer (see Supplementary Fig. S5). b, A schematic of the MAG/Si device shows the charge transport and current flow. c, HR-TEM image of the MAG/Si showing an atomic-scale contacting interface (see Supplementary Fig. S6). The highly aligned (002) lattice fringes and corresponding sharp discrete spots in the fast-Fourier-transform (FFT) pattern indicate a highly ordered structure of MAG with the interlayer space of $3.36 \pm 0.04 \text{ \AA}$, consistent with the result of GI-WAXS. d, Cross-sectional TEM image of MAG/Si with Pt layer on the top for protection during focused-ion-beam (FIB) milling (see Supplementary Fig. S7). e, The Fourier-transform-infrared-spectroscopy (FTIR) extinction spectra ($1-T/T_0$) of SLG/Si and MAG/Si from 1 to 10 μm , where T is the transmission through MAG/Si and SLG/Si, and T_0 is the transmission only through Si substrate underneath (see Supplementary Fig. S9). f, The NSD $S(f)/I_{\text{dark}}^2$ as a function of frequency at a different reverse bias of MAG/Si (see Supplementary Fig. S10a, b). The window size is 2 mm \times 2 mm. g, The direct-current I-V curves of MAG/Si under dark, and laser illumination at 2 μm , 4 μm , and 10 μm wavelength with 200 fs pulse width, 100 kHz repetition rate and 50 mW mm^{-2} irradiances. All the scanned I-V curves showed negligible hysteresis indicating a clean MAG/Si interface.

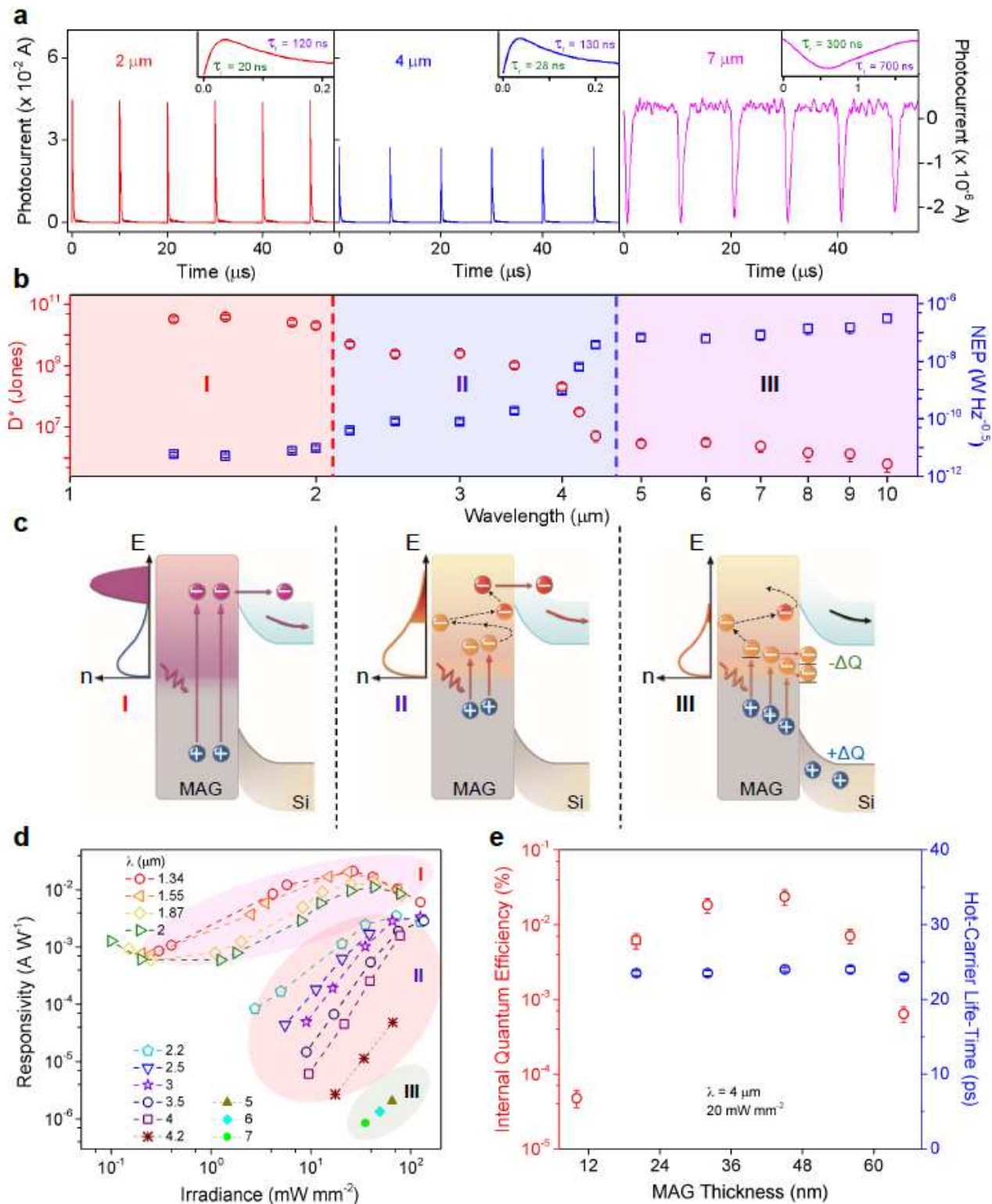


Figure 3

Transient photoresponse of MAG/Si. a, The photocurrent of MAG/Si in time domain under pulsed-laser (200 fs of pulse width, 100 kHz of repetition rate) illumination at 2 μ m, 4 μ m, and 7 μ m wavelength with a 50 mW mm^{-2} irradiance. The photocurrent in the vertical axis at 4 μ m is on the same scale as at 2 μ m on the left (see Supplementary Fig. S11, 12, Video S1). Insets show the corresponding single periods. b, The D^* and NEP of MAG/Si as a function of laser wavelength under a fixed irradiance of 10 mW mm^{-2} (see

Supplementary Fig. S14a-c). c, the corresponding energy-band diagrams for operation mechanism at the three wavelengths above. d, The responsivity of MAG/Si as a function of laser irradiance at different wavelengths. e, The internal-QE and hot-carrier life-time of MAG/Si as a function of MAG thickness at 4 μm laser wavelength with a fixed irradiance of 20 mW mm^{-2} (see Supplementary Fig. S15).

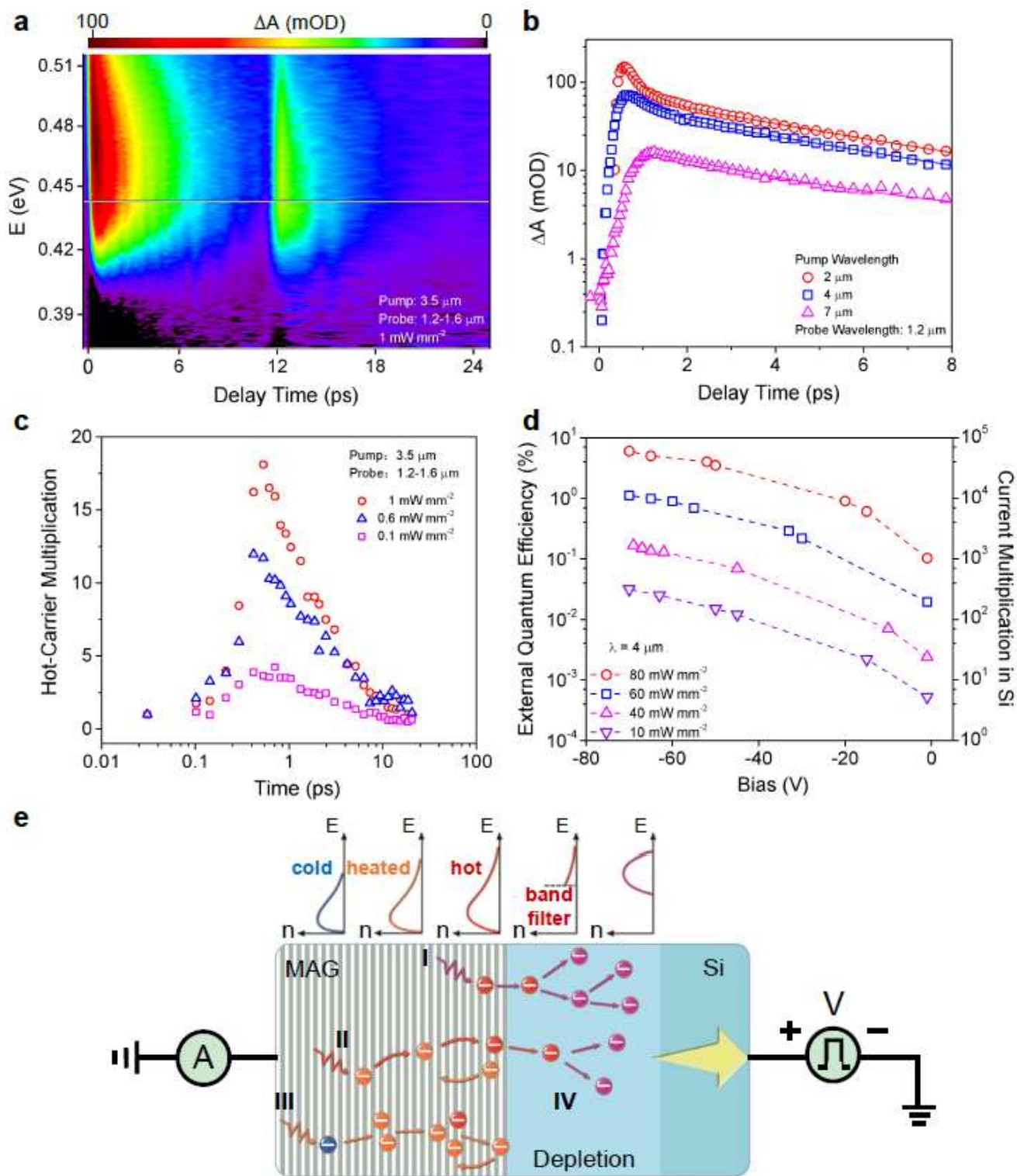


Figure 4

Hot-carrier transport in MAG/Si. a, 2D transient absorption map of MAG/Si as functions of delay time and the half of incident photon energy (the mOD means milli-optical density). The sample is pumped at $3.5\ \mu\text{m}$ with an irradiance of $1\ \text{mW mm}^{-2}$. The second peak at $\sim 10\ \text{ps}$ is due to photo-excitation from the reflected pump laser on the silicon substrate (thickness of $500\ \mu\text{m}$) underneath. b, The transient-absorption kinetics probed at $1.2\ \mu\text{m}$ with a pump at $2\ \mu\text{m}$, $4\ \mu\text{m}$, and $7\ \mu\text{m}$ (see Supplementary Fig. S18). c, The hot-carrier multiplication factor as a function of time under different pump irradiance at $3.5\ \mu\text{m}$ and probed in the range from 1.2 to $1.6\ \mu\text{m}$. d, The external-QE and current amplification factor as a function of bias V_b of MAG/Si under $4\ \mu\text{m}$ wavelength laser with different irradiance (see Supplementary Fig. S19, Video S2). e, The operation mechanism schematic of MAG/Si photodiode under $2\ \mu\text{m}$ (I), $4\ \mu\text{m}$ (II), and $7\ \mu\text{m}$ (III) photo-excitations and avalanche (IV).

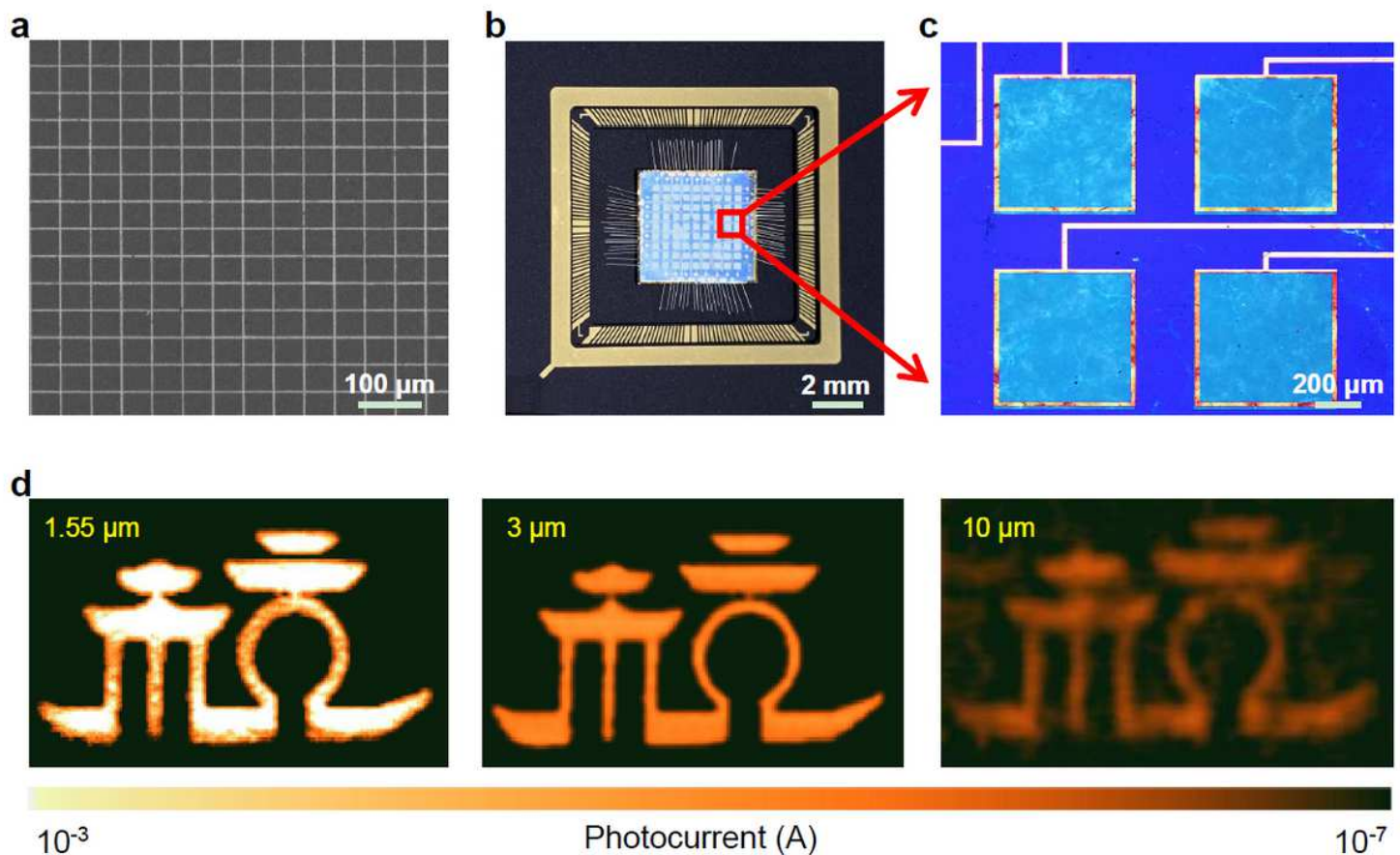


Figure 5

MAG/Si image sensors. a, A SEM image shows the plasma etched MAG pixel array on silicon with a dimension of $50\ \mu\text{m} \times 50\ \mu\text{m}$ for each pixel (see Supplementary Fig. S20). b-c, A photo of 9×9 packed MAG/Si image sensor with the zoomed-in optical image. d, The scanned images of a Chinese character “杭 (Hang)” representing the Hangzhou city at $1.55\ \mu\text{m}$, $3\ \mu\text{m}$, and $10\ \mu\text{m}$ laser wavelength (see Supplementary Fig. S21). The color bar represents the photocurrent level.

Supplementary Files

This is a list of supplementary files associated with this preprint. Click to download.

- [SupplementaryInformation.pdf](#)
- [SupplementaryVideoS1.mp4](#)
- [SupplementaryVideoS2.mp4](#)